Optical spin injection in MoS$_2$ monolayers

N. Arzate,[*] Bernardo S. Mendoza, and R. A. Vázquez-Nava
Centro de Investigaciones en Óptica, León, Guanajuato, Mexico

Z. Ibarra-Borja
División de Ciencias e Ingenierías, Universidad de Guanajuato, Mexico

M. I. Álvarez-Núñez
Ingeniería en Nanotecnología, Universidad de La Ciénega del Estado de Michoacán de Ocampo, Mexico

Two-dimensional transition-metal dichalcogenide materials have recently attracted great attention from the scientific community due to their interesting properties such as the presence of an energy band gap and the support of spin-polarized states. In particular, monolayer molybdenum disulfide has a structure with no inversion symmetry and, thus, presents a large spin-splitting of the top valence bands. This latter fact makes it favorable for studies of optical spin injection, a phenomenon that, under incidence of circularly polarized light, creates spin-polarized electrons in the conduction bands. Here, we perform a theoretical study of the one-photon optical spin and current injection on transition-metal dichalcogenide monolayers of molybdenum disulfide. In particular, we present calculations for spectra of the degree of spin polarization, which are calculated in a full-band structure scheme employing density functional theory; besides the so-called quasiparticle GW approximation is applied for the calculation of the band gap energy correction. Our results show 100% of spin polarization of the electrons for the one monolayer structure at the **K** valley. The degree of spin polarization also presents a net maximum value at the direct energy band gap at **K** as the number of monolayers increases.

I. INTRODUCTION

The monolayers of molybdenum disulfide (MoS$_2$) are two-dimensional (2D) transition-metal dichalcogenide materials that have recently attracted great attention from the scientific community [1]. Their formation has been realized through the use of a mechanical exfoliation technique [2,3]. Unlike graphene, monolayers of MoS$_2$ offer not only the advantage of having a band gap but also of supporting spin polarized states, which is suitable for many applications in electronics, photonics, spintronics, and in the most recent research field of valleytronics. The latter field relies on the fact that in the band structure of semiconductor materials, the minimum conduction band, at a different wave vector or momentum, can have two or more minima at equal energies [4]. This represents another degree of freedom which can be used in order to control the number of carriers that are taken to the conduction band within these valleys.

Studies of spin polarization in monolayers of MoS$_2$ have been performed. For instance, some studies have found that inversion symmetry breaking along with spin-orbit coupling (SOC) leads to coupled spin and valley physics in monolayers of MoS$_2$ and other group-VI dichalcogenide compounds [3,5–7]. Very recently, Muniz and Sipe have perturbatively computed the optical injection rates of charge, spin, and valley densities and currents in monolayer transition-metal dichalcogenides, for an incident optical field in addition to its second harmonic [8]. They have verified that the interference of one- and two-photon absorption processes allows for the

injection of currents, resulting in an all-optical method for current injection.

In the present paper, we have studied the phenomenon of one-photon optical spin injection on monolayers of MoS$_2$ structures. Optical spin injection of carriers takes place when circularly polarized light falls on a semiconducting material and injects spin-polarized electrons from the valence into the conduction bands [9]. The electron spin polarization takes place as a result of the interaction of the electron spin and motion caused by the SOC in the material. The feasibility of optical spin injection into nonmagnetic materials has already been studied in bulk GaAs, Si, CdSe, and Ge semiconductors [10–12], as well as at adsorbate-covered Si(111) and GaAs(110) surfaces [13,14]. The fraction of injected electrons into the conduction bands that are spin-polarized along the light propagation vector is given by the degree of spin polarization (DSP). The formalism for its calculation has been developed within the independent particle approximation and following the Fermi's golden rule approach [10,11]; it has also been applied and incorporated into surfaces and interfaces [14].

Furthermore, we have also studied the optical generation of injection current, which is a second-order nonlinear effect that takes place in noncentrosymmetric crystals [15–22]. An observable photocurrent can be injected with a single optical beam and arises from the interference of one-photon absorption processes associated with different linear polarizations of the light [17,18,22]. Incidence of circularly polarized light onto a noncentrosymmetric crystal leads to different excitation pathways for the two orthogonal polarization components, resulting in an interference effect. An asymmetric population of the injected carriers, in turn, takes place in reciprocal space, which leads to an injection current. In the process of current injection, the energy increase of the injected carriers

---

*narzate@cio.mx

115433-1

is provided by the electromagnetic field, while the increase in momentum is provided by the crystal lattice.

Our motivation to carry out optical spin injection studies on monolayer MoS_2 structures is the fact that one-monolayer MoS_2 has been found to be a promising material for valleytronics applications [7]. In particular, it has been reported that the DSP reaches the value of 100% at the valley located at the **K** and **K**′ wave vectors [23]. Here we perform such a calculation for the DSP in the whole Brillouin zone (BZ) by applying a full-band structure scheme. Thus we have obtained spectra for the DSP for bulk and n-monolayer MoS_2 structures. Besides, we also present calculations for the optical injection of current under incidence of one circularly polarized optical beam.

The organization of the paper is as follows. We give, in Sec. II, details of the atomic structure of bulk and monolayer MoS_2. We explain briefly, in Sec. III, the theory of optical spin and current injection. In Sec. IV, we describe the method employed for the calculations. We show, in Sec. V, corresponding spectra for the DSP and injection current. And, finally, we give conclusions in Sec. VI.

II. STRUCTURE

The 2H-MoS_2 structure belongs to the transition-metal dichalcogenide family. Its bulk structure is characterized by an hexagonal-layered lattice or graphenelike arrangement wherein, within each layer, molybdenum (Mo) and sulfur (S) atoms bind together forming S-Mo-S units in such a way that an atomic plane of Mo atoms is sandwiched by two atomic planes of S atoms forming a trigonal prismatic arrangement or ABAB stacking (see Fig. 1).

Each Mo (S) atom bonds to six (three) S (Mo) atoms. The space group of bulk MoS_2 is $P6_3/mmc$. There are two S-Mo-S units within each bulk unit cell. Those layers are bound by weak van der Waals forces. In Fig. 1, we can see the top and side views of the MoS_2 bulk structure. The quadrangles shown in panels (a) and (c) of Fig. 1 indicate the respective bulk unit cell.

On the other hand, the one-monolayer MoS_2 is characterized by being formed by one S-Mo-S unit within its lattice unit cell. It belongs to the space group $P\bar{6}m2$ and has no inversion symmetry. In general, the n-monolayer MoS_2 structure contains n S-Mo-S units within its lattice unit cell and has no inversion symmetry if n is odd; in contrast, it does
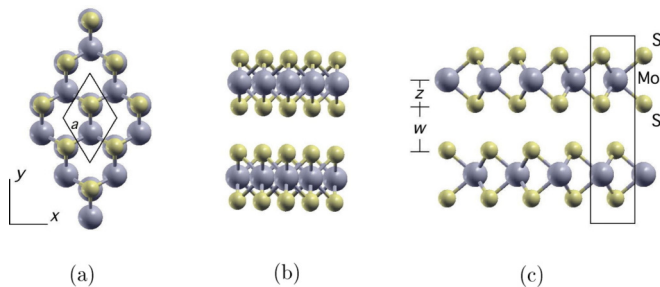

FIG. 1. (a) Top and (b),(c) side views of the bulk structure of MoS_2. The rectangles in panels (a) and (c) show the unit cell, with a being the lattice constant. In panel (c), z and w indicate the interatomic and interlayer distances along z, respectively.
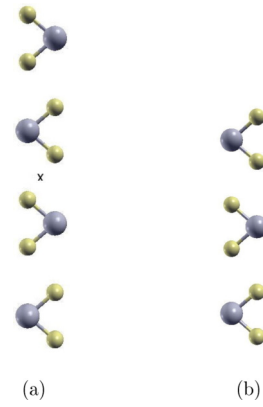

FIG. 2. Side views of the S-Mo-S units forming the unit cells of (a) the four- and (b) three-monolayer structures, respectively. The cross in the four-monolayer structure indicates its respective point of inversion of symmetry.

have inversion symmetry if n is even. This fact is exemplified in Fig. 2, wherein four- and three-monolayer MoS_2 structures are shown.

III. THEORY

A. Optical spin injection

The study of the optical spin injection has been performed through calculations of spectra of the DSP along direction a, $\mathcal{D}^a$, which is obtained by the ratio [10]

$$\mathcal{D}^a = \frac{\dot{S}^a}{(\hbar/2)\dot{n}}, \qquad (1)$$

where $\dot{S}^a$ is the spin injection rate along direction a, which for one photon absorption is given by

$$\dot{S}^a = \zeta^{abc}(\omega)E^b(-\omega)E^c(\omega), \qquad (2)$$

where $E^i(\omega)$ is the optical electric field as a function of photon frequency ω along direction i. And $\zeta^{abc}(\omega)$ is a third-rank pseudotensor called spin injection tensor, which is given by [10]

$$\zeta^{abc}(\omega) = \frac{2\pi e^2}{\hbar^2} \sum_{c,c',v} \int \frac{d\mathbf{k}}{8\pi^3} \mathcal{S}^a_{c'c}(\mathbf{k}) r^b_{vc'}(\mathbf{k}) r^c_{cv}(\mathbf{k})$$
$$\times (\delta[\omega_{cv}(\mathbf{k}) - \omega] + \delta[\omega_{c'v}(\mathbf{k}) - \omega]). \qquad (3)$$

Here, the physical constants e and $\hbar$ are the electron charge and Planck constant divided by 2π, respectively. The integral is performed over the BZ, and the sum is carried out over all valence v and c conduction bands; c' runs over conduction bands that are quasidegenerate with c bands. That is, Eq. (3) takes into consideration excited coherences of spin split conduction bands due to a pulse excitation of a coherent superposition of two conduction bands. Besides, $\omega_{cv}(\mathbf{k}) = \omega_c(\mathbf{k}) - \omega_v(\mathbf{k})$ gives the transition energies between the states $|c\mathbf{k}\rangle$ and $|v\mathbf{k}\rangle$ of the system; $\mathcal{S}^a_{c'c}(\mathbf{k})$ and $r^a_{vc}(\mathbf{k})$ are the spin and position matrix elements, respectively. The pseudotensor $\zeta^{abc}(\omega)$ is imaginary and changes sign under exchange of the last two indices.

On the other hand, $\dot{n}$ is the carrier injection rate defined by

$$\dot{n} = \xi^{ab}(\omega)E^a(-\omega)E^b(\omega), \tag{4}$$

where the tensor $\xi^{ab}(\omega)$ is related to the imaginary part of the linear optical response tensor and is expressed by [10]

$$\xi^{ab}(\omega) = \frac{2\pi e^2}{\hbar^2} \int \frac{d\mathbf{k}}{8\pi^3} \sum_{c,v} r_{vc}^a(\mathbf{k}) r_{cv}^b(\mathbf{k}) \delta[\omega_{cv}(\mathbf{k}) - \omega]. \tag{5}$$

In the calculations, we consider normal incidence of circularly polarized light propagating along the $-z$ direction, $\mathbf{E}(\omega) = E_0(\hat{x} - i\hat{y})/\sqrt{2}$, being E_0 the field intensity. Since $\mathbf{E}(\omega)$ lies on the plane of the surface, it can be taken, with the usual neglect of local field corrections, as uniform through the interface region.

It is worth mentioning that, in MoS₂ monolayers, the interplay of inversion of symmetry breaking and the SOC gives rise to a valley-dependent optical selection rule that allows interband transitions in the vicinity of the wave vector $\mathbf{K}$ ($\mathbf{K}'$) point by a selective coupling to right (left)-handed circularly polarized light, respectively. The fact that the optical selection rule only applies close to the $\mathbf{K}$ ($\mathbf{K}'$) implies that the frequency of the optical field that is used to excite the sample must be close to that of the direct transition frequency at $\mathbf{K}$ (or $\mathbf{K}'$), i.e., in resonance condition. Otherwise, if excitation is far away from resonance then the valley optical selection rule relaxes, allowing the electron population in both $\mathbf{K}$ and $\mathbf{K}'$ valleys [24,25].

B. Optical current injection

The one-photon injection current is defined, in the independent particle approximation, as [18]

$$\dot{\mathbf{J}}_a^{\text{inj}}(\omega) = 2\eta^{abc}(\omega)E^b(\omega)E^c(-\omega). \tag{6}$$

The factor of 2 in Eq. (6) takes into account contributions of a field with frequency components ω and $-\omega$. Here, $\eta^{abc}(\omega)$ is the injection current tensor, which quantifies the injection current along direction a that is optically injected by incident light circularly polarized on the plane defined by directions b and c. It is given by [18]

$$\eta^{abc}(\omega) = \frac{e^3\pi}{2\hbar^2} \int \frac{d\mathbf{k}}{8\pi^3} \sum_{n,m} \Delta_{mn}^a f_{nm} [r_{mn}^c, r_{nm}^b] \delta(\omega_{mn}(\mathbf{k}) - \omega), \tag{7}$$

where the integral is performed over the BZ and the sum is carried out over all m and n bands. Here, $\Delta_{mn}^a = v_{mm}^a - v_{nn}^a$ with v_{mn}^a being the velocity matrix elements, $f_{nm} = f_n - f_m$ with f_n being the Fermi factor, and $[r_{mn}^c, r_{nm}^b] = r_{mn}^c r_{nm}^b - r_{mn}^b r_{nm}^c$. $\eta^{abc}(\omega)$ is purely imaginary and is antisymmetric in its last two Cartesian indices. Since it is a third rank tensor, $\eta^{abc}(\omega)$ is different from zero in those crystals that lack inversion symmetry. There are 21 crystal classes without a center of inversion symmetry, but only in 18 of those, $\eta^{abc}(\omega)$ does not vanish, except for crystals with point groups $\bar{6}m2$, $\bar{6}$, and $\bar{4}3m$. $\eta^{abc}(\omega)$ vanishes for optical excitation below the band gap energy.

IV. METHOD

We have performed numerical calculations for $\mathcal{D}^z$ and η^{xyx} for bulk and n-monolayer MoS₂ structures. For our calculations, we have considered monolayer systems of MoS₂ consisting of one, two, three, and five monolayers. We have modeled the monolayer structures through a supercell approach, wherein a vacuum length of at least 10 Å was considered. The experimental bulk lattice constants were used for the calculation [26]: $a = 3.16$ Å and $c = 12.296$ Å. The interatomic and interlayer distances employed were $z = 1.565$ Å and $w = 3.018$ Å. We have assumed this approximation for the lattice constant since, on the one hand, it has been reported that the experimental bulk lattice constant of MoS₂ well reproduces the band gap of the monolayer MoS₂ structure [27]; on the other hand, energy minimization calculations have shown that the lattice constant of monolayer and bilayer MoS₂ structures are perfectly in accord with the experimental bulk value [26,28]. In particular, the corresponding calculations of Debbichi *et al.* [28] took into account the weak van der Waals interaction that is present in these structures. They found that the in-plane lattice constant was perfectly in accord with the corresponding experimental bulk value, while the interlayer distance differed in only 2% from the experimental bulk value [28].

In order to obtain the momentum matrix elements required in an optical response calculation, we have performed *ab initio* pseudopotential calculations in the framework of density functional theory (DFT) within the local density approximation (LDA), with the use of the plane-wave ABINIT code [29]. The ground state was calculated in a grid of $\mathbf{k}$ points of $10 \times 10 \times 6$ and $8 \times 8 \times 1$ for bulk and n-monolayer MoS₂ structures, respectively. We have taken a cutoff energy of 40 Ha for the plane wave expansion of the wave functions and used the relativistic separable dual-space Gaussian pseudopotentials of Hartwigsen-Goedecker-Hutter [30], which take into account the spin-orbit interaction needed in spin-polarization calculations. In the atomic pseudopotential, six valence electrons, of character s and p, were taken for S atoms; meanwhile, six valence states, of s and d character, were only considered for Mo atoms.

It is worth mentioning that the inclusion of spin-orbit interaction in the calculation of the quasiparticle energies can be done through three different approaches. In the first approach, the SOC is fully taken into account in the first iteration GW calculation of the noninteracting reference system. Hence spin-orbit interaction is naturally included in the single-particle Green function, the screened interaction, and the self-energy; in this approach, both spin-orbit screening and renormalization effects in spin-orbit split bands are taken into account [31,32]. The second approach also considers a full treatment of the SOC just like in the first; in this case, however, the inclusion of the SOC is only considered in the Green function, and it is neglected in the screened Coulomb potential. The use of either of these two approaches is very important for cases where accurate results are required, such as in topological insulators or systems with small band gaps [31–34]. The third approach incorporates the SOC by using the so-called second variation [35], i.e., after the quasiparticle correction to the Kohn-Sham energies has been performed. Here, SOC is included in the LDA calculation, yielding

relativistic LDA eigenstates. Hence the scalar-relativistic LDA eigenvalues are replaced by the quasiparticle energies that are obtained in the calculation without SOC. Aguilera *et al.* noted that this approach is only applicable in cases where the Kohn-Sham states are reasonable approximations for the respective quasiparticle amplitudes without SOC [32]. This last approach makes the GW calculations faster than those of the first two, since spinor wave functions are not employed.

In a full-band structure optical-response calculation, the evaluation of the quasiparticle energies in the whole BZ is required. This is still a time-demanding task. Instead, a scissors approach has been used, where the LDA conduction bands are rigidly shifted by an energy value equal to the G_0W_0 energy correction [36,37]. Peelaers *et al.* [38] tested the validity of the scissors approach in Si and Ge nanowires and found that the scissors approach is a valid approximation for **k** points close to the band gap region and for bands close to the highest valence and lowest conduction bands.

In the present study, as discussed in the previous two paragraphs, we incorporate the SOC through the use of the second variation approach and the scissors approximation. Hence, in order to correct the underestimation of the energy band gap of the LDA calculation, we have performed a many-body first iteration G_0W_0 calculation just at the Γ point. Convergence of the GW band gap to within 0.01 eV was reached with cutoff energies of 30 and 20 Ha, 134 and 152 conduction bands, and with **k** grids of $20 \times 20 \times 16$ and $52 \times 52 \times 1$ for the bulk and one-monolayer MoS_2 structures, correspondingly. The plasmon pole approximation for the screening potential was employed for the calculation of the quasiparticle energies. The optical responses, $\mathcal{D}^z$ and η^{xyx}, were calculated by reaching convergence in the number of **k** points in the irreducible BZ of 2912 and 392 for bulk and monolayer MoS_2 structures, respectively.

We mention that monolayer atomic structures might have large excitonic effects which, in turn, could modify their optical properties such as optical response tensors. In the literature, we can find few reports of calculations of quasiparticle band structure and optical properties of monolayer MoS_2 including electron-electron and electron-hole interactions, which is done by using the Bethe-Salpeter equation [39–44]. These reports, for instance, show that the respective calculated optical band gap value is consistent with experimental results. The inclusion of excitonic effects in the calculation of electronic and optical properties of 2D systems still remains a numerical challenge. This task is beyond the scope of the present theoretical study.

V. RESULTS

A. Band structure

The monolayer MoS_2 system has been shown to be a challenging system for calculating its electronic and optical properties. In the literature, we can find many studies that calculate the electronic band structure of bulk and monolayer MoS_2 by using DFT, GW, and Bethe-Salpeter equation (BSE) approaches [26,28,39–45]. In those reports, we found that, for instance, there are variations of the corresponding GW calculated values of the band gap depending on the approximation used. The origin of all those discrepancies is still not clear at all, and further research in this direction is necessary. Here, we show calculated electronic band structures for the studied monolayer MoS_2 systems in order to show the consistency of our calculated band gap results among them for the different monolayer structures (see Table I), and have a comparison with either experiments or previous calculations.

We show, in Fig. 3, band structures calculated by using the DFT-LDA plus GW band gap energy correction. for the bulk, bilayer, and monolayer MoS_2 systems. In the calculations,

TABLE I. Calculated splitting of the two top branches of degenerate valence bands, G_0W_0 energy correction ΔE_g, and their respective G_0W_0 energy band gap E_g, for bulk and monolayer (ml) MoS_2 structures. The label I (D) stands for the indirect (direct) energy band gap. Note that our calculated direct band gap values compare rather well with respect to the experimental values.

MoS_2 structure	Splitting (meV)	ΔE_g (eV)	E_g (eV)					
			Ours		Experiment[a]		Theory	
			I	D	I	D	I	D
Bulk	231	0.11	0.97	1.79	1.29	1.88	0.9,[b] 0.88[c] 1.3,[d]	
5 ml	133	0.05	0.99	1.74	1.38	1.85		
3 ml	135	0.08	1.14	1.77	1.46	1.87	1.59[d]	
2 ml	166	0.19	1.45	1.90	1.59	1.88	1.30,[b] 1.25[c] 2.00,[d] 1.83[e]	
1 ml	137	0.21		1.93		1.90		1.70,[b] 1.77,[c] 2.77[f] 2.84,[g] 2.80,[h] 2.76[i]

[a]Experimental energy band gaps for bulk and monolayer structures were taken from Refs. [47] and [3], respectively.
[b]DFT calculation [45].
[c]DFT calculation [26].
[d]G_0W_0 calculation [39].
[e]G_0W_0 calculation [28].
[f]G_0W_0 calculation [42].
[g]G_1W_0 calculation [44].
[h]Self-consistent GW_0 calculation [43].
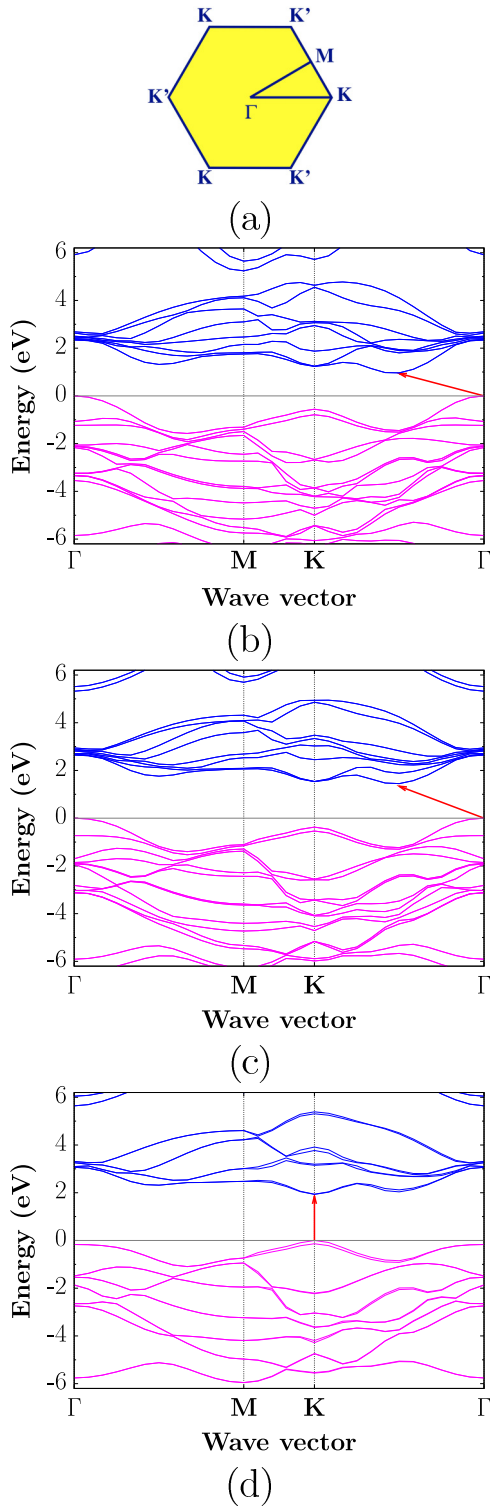[i]Self-consistent GW calculation [40].

(a)

(b)

(c)

(d)

FIG. 3. (a) Brillouin zone for the monolayer MoS₂ structure. (b) Band structures of bulk, (c) bilayer, and (d) one-monolayer MoS₂ structures. Spin-orbit interaction was taken into account in the calculation. The arrows indicate the indirect (b) and (c) or direct (d) band-gap transitions, which take place from the highest valence band to the lowest conduction band. The corresponding GW band gap energy correction has been applied.

spin-orbit interaction was taken into account. We can observe from Fig. 3 that the bulk and two-monolayer MoS₂ structures
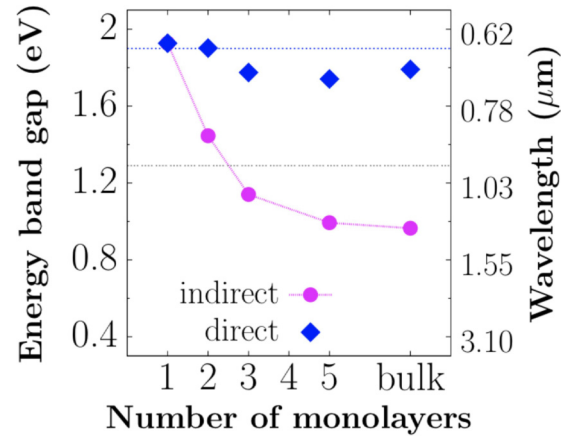

FIG. 4. Calculated GW-energy band gap for different monolayer MoS₂ structures containing n monolayers. The circle (diamond) dots indicate the indirect (direct) energy band gaps. The dotted lines show the experimental energy band gaps for the bulk (at 1.29 eV) and monolayer (at 1.9 eV) MoS₂ structures.

present an indirect fundamental energy band gap, which corresponds to indirect transitions that take place from the maximum of the highest valence band at Γ and to the minimum of the lowest conduction band at a **k** point that is along the **K**-Γ path, whereas the fundamental energy band gap of the MoS₂ monolayer is direct and has a GW-calculated value of 1.93 eV. This direct energy band gap corresponds to direct transitions that take place from the maximum of the highest valence band to the minimum of the lowest conduction band at the **K** wave vector. We have also obtained band structures for three- and five-monolayer MoS₂ structures. We tabulate in Table I and show in Fig. 4 the GW-calculated values of the indirect and direct energy band gaps for the bulk and the different n-monolayer MoS₂ structures. The bulk structure as well as n-monolayer MoS₂ (with $n > 1$) structures have an indirect energy band gap, and the MoS₂ structure becomes a direct band gap semiconductor when the MoS₂ structure has only one monolayer. This behavior of the band gap is in accord with photoluminescence experiments [3,46]. We can see from Table I that the calculated indirect band gap values for the bulk and n monolayers of MoS₂, with $n > 1$, are underestimated in comparison with the experimental values; in contrast, it is worth noting that the calculated direct-band gap values for the monolayer and bilayer structures are in very good agreement with those found in photoluminescence experiments [3], Meanwhile, the corresponding direct energy band gaps for the three and five monolayers of MoS₂ are comparable and slightly below the corresponding experimental values. All those direct energy band gaps have their respective value at around the experimental value for the monolayer MoS₂ structure.

The large overestimation of the band gap found in previous GW calculations in the monolayer MoS₂ system has been attributed to the fact that, in finite 2D systems, there is an additional contribution to the screen potential coming from a screening charge that is repelled on the surface. This corresponds to a macroscopic surface polarization charge that gives an additional contribution to the self-energy correction [48]. The very good agreement of our calculated GW band

gap with that of the experiment seems to be remarkable. Such an agreement with those of the experiment remains for the respective band gap calculations of the other two, three, and five monolayer MoS2 structures, showing consistency of our results among them. In order to elucidate the origin of this fact we note that the GW band structures for monolayer MoS2 converge very slowly with respect to the interlayer separation [39,42]. Besides, Hüser *et al.* stated that the use of a truncated Coulomb interaction is necessary, along with a **k**-point grid of around $45 \times 45 \times 1$ [42]. Komsa *et al.* calculated the band gap energies for bulk and few-layer MoS2 as a function of the inverse of the interlayer distance and found that, at the GW level, the direct band gap increases as the interlayer distance increases due to the nonlocal nature of the GW approximation [39]. All their calculated values overestimate the experimental band gap of the monolayer. In their calculations, they found a value of 2.30 eV for the direct band gap with a value of the inverse of the interlayer distance of 0.1 AA^{-1}. The value of the band gap keeps increasing as the interlayer distance approaches infinity, reaching the limiting and extrapolated value of 3.0 eV. This result suggests that very large supercells are necessary to obtain more accurate GW band gap calculations. However, the use of large supercells in the normal direction to the monolayer is computationally prohibited. This fact might partly explain the variations in the reported GW band gap values. Here, in order to reduce the computational cost, we have opted to keep the inverse interlayer distance at the value of 0.1 AA^{-1}, and we have obtained convergence of the band gap with the number of the **k** points, reaching the **k** point grid suggested by Hüser *et al.* [42]. An increment of the interlayer distance will increase the GW band gap and, in turn, the calculated optical spectra will be just rigidly shifted by such an increment.

Furthermore, from Figs. 3(b) and 3(c), we can observe that both band structures, that corresponding to the bulk and that corresponding to the bilayer MoS2 structure, show spin degeneracy of the valence and conduction bands due to the inversion symmetry that is present in both structures. On the other hand, we can see from Fig. 3(d) that the SOC makes the two top valence bands of the monolayer MoS2 structure be spin-split at around the **K** point, reaching a maximum splitting of 137 meV. The two top valence bands obey the constraint of time reversal symmetry at **K** and **K**′, $E(\mathbf{k},\uparrow) = E(-\mathbf{k},\downarrow)$, where $\uparrow$ and $\downarrow$ indicate spin-up and spin-down polarization at the **K** point, respectively. However, those bands are spin degenerate at the Γ and M points, due to time reversal invariance. In general, the respective band structures of the n-monolayer MoS2 structures show two top degenerate valence band branches, which have a number of degenerate bands equal to the number of layers. Table I also shows the energy difference between each of these two valence band branches for each of the studied structures. Such energy difference is due to the spin-orbit splitting of the valence bands and leads to two absorption resonances, which have been identified as direct excitonic transitions at the **K** point [46,49]. The finding of the splitting of the valence-band maximum of single and few monolayer MoS2 structures is in accord with recent photoluminescence measurements performed at different temperatures [50].

B. Spin injection

Zhang *et al.* have demonstrated the existence of a compensated (hidden) spin polarization in centrosymmetric crystals by first-principles calculations [51,52]. They showed that the local symmetry or site point group determines the presence of spin-orbit interaction in a material, instead of the bulk symmetry or space group. We can understand this by considering a layered crystal that has inversion symmetry in the bulk, but not locally. Then, each of its layers has a local symmetry that produces a local dipole field which leads to a local Rashba spin polarization [53], or a site asymmetric field which leads to local Dresselhaus spin polarization [54]. The combination of a bulk centrosymmetric space group with a site dipole field or site inversion asymmetry leads to spin polarizations called R-2 and D-2 effects, respectively [51]. In the compensated R-2 spin polarization, the spin polarization from each local layer is compensated by another one that is called inversion partner. Thus the R-2 spin polarization is concealed by compensation. Although all energy bands must be degenerate in centrosymmetric materials, Zhang *et al.* found that the two pairs of degenerate valence and conduction bands could have opposite polarizations, each spatially localized on one of the two layers, whose spin polarization is mutually compensated. Physically, the effective magnetic field generated due to the motion of the charge carriers is proportional to the local gradient of the electric potential [52]. In centrosymmetric systems, this electric field does not vanish at all atomic sites. In bulk centrosymmetric crystals, the R-2 spin polarization effect is accompanied by the D-2 spin polarization effect. They can occur in crystal structures with space groups $P6_3/mmc$ (for example, MoS2), $R\bar{3}m$, and $P4/nmm$ [51]. Here, we have calculated spectra for $\mathcal{D}^z$ for both centrosymmetric and noncentrosymmetric MoS2 structures. Thus, according to the studies of Zhang *et al.*, it might be expected that, in both these kinds of structures, there would be a net spin polarization.

We show, in Fig. 5(a), spectra of $\mathcal{D}^z$ for bulk and n-monolayer MoS2 structures, with $n = 1,2,3,5$, under incidence of circularly polarized light. We have used a Gaussian smearing of 25 meV in the spectra in order to account for population decay and dephasing. We have chosen this value since it corresponds to the room-temperature broadening of the energy bands. The $+(-)$ sign on the $\mathcal{D}^z$ spectrum indicates that spin polarization is along the $+(-)$ z direction. We can see that, for the first-monolayer MoS2 structure, $\mathcal{D}^z$ reaches its maximum value of -1 at 2.01 eV, which means that 100% of the electrons that are injected to the conduction bands are spin polarized. The values of $|\mathcal{D}^z|$ keep above 0.9 within an energy interval width of 100 meV, as it can be seen in the inset of Fig. 5(a). In Fig. 5(b), we plot the maximum values of $\mathcal{D}^z$ for each of the studied MoS2 structures. Such maxima correspond to transitions that take place just around **K** or **K**′ points, with energies around the direct band gap value. We observe that $\mathcal{D}^z$ decreases as the number of monolayers of the MoS2 structure increases. It is the expected behavior; that is, as the number of monolayer gets a large value, $\mathcal{D}^z$ reaches its respective bulk value. Our result of maximum 100% of spin polarization at **K** for the monolayer MoS2 structure is in accord with that obtained by Chang *et al.* [23]. However, we have found contrasting results for the behavior of the maximum
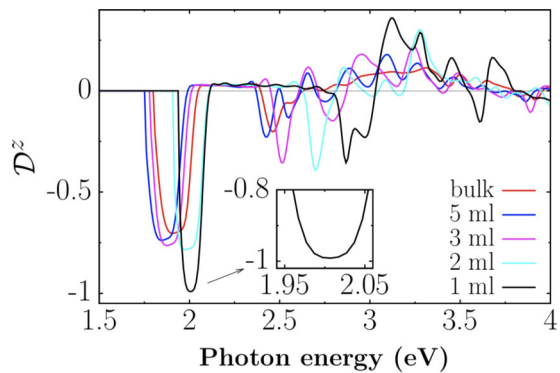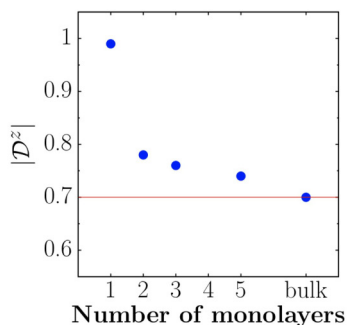
FIG. 5. (a) Spectra of the degree of spin polarization $\mathcal{D}^z$ along direction z for bulk and n-monolayer MoS₂ structures, under incidence of circularly polarized light. (b) Corresponding maximum $\mathcal{D}^z$ values.

of $\mathcal{D}^z$ as a function of the number of monolayers. Such a difference might be understood from the fact that they did not consider the existence of the compensated spin polarization in centrosymmetric structures, and thus expressed the behavior of $\mathcal{D}^z$ as inversely proportional to the number of monolayers for MoS₂ structures with an odd number of monolayers. Chang *et al.* reported that, for MoS₂ structures with an even number of monolayers, $\mathcal{D}^z$ is zero, since the system is centrosymmetric; and that, for MoS₂ structures with and odd number of monolayers, the value of $\mathcal{D}^z$ at **K** tends to zero as the number of monolayers gets large, and thus a bulk structure is formed, whereas our results show that the maximum of $\mathcal{D}^z$ decreases from 100% to 70% as the system goes from a monolayer to a bulk structure. In both centrosymmetric and noncentrosymmetric monolayer structures, $\mathcal{D}^z$ is different from zero.

Mak *et al.* have reported polarization-resolved photoluminescence spectra of monolayer and bilayer MoS₂ structures. They excite the sample on resonance with the exciton at 1.96 eV, and quantify the degree of photoluminescence polarization by the helicity parameter determined by intensities of right and left circularly polarized light [3]. They found that the helicity parameter has values at around 1.00+0.05 for photon energies in the range 1.90–1.95 eV, and drops rapidly to 0.05 below 1.8 eV. This observation is indicative of the valley-dependent optical selection rule that applies at photon

TABLE II. Comparison of some reported percentage values for $|\mathcal{D}^z|$ for surface and bulk systems.

Structure	Energy (eV)	$|\mathcal{D}^z|$ (%)	Reference
1 ml MoS₂	2.01	100	This work
Bulk MoS₂	1.91	70	This work
Bulk CdSe	1.80	100	[10]
Bulk GaAs	1.50	50	[10,16]
Bulk Ge	0.90	50	[12]
Bulk Si	3.44	30	[10]
Si(111)-As 1 × 1	2.20	100	[14]
GaAs(110)-clean 1 × 1	1.64	90	[14]

energies nearby the direct band gap or wave vector **K** or **K′** for the noncentrosymmetric monolayer MoS₂ structure. In the inset of Fig. 5(a), we can see that within an energy interval of 0.05 at around the energy corresponding to the maximum value of the spectrum, $|\mathcal{D}^z| > 0.97$. Hence the monolayer MoS₂ structure presents valley spin polarization at **K** with almost 100%. Under excitation by left circularly polarized light, spin polarization at the **K′** valley takes place and $\mathcal{D}^z$ would have the same magnitude, but with opposite direction. This reversal in sign is due to the time reversal symmetry that results in a change of sign in the spin matrix elements for the calculation of the spin generation rate. In contrast, in the two-monolayer MoS₂ structure, the inversion symmetry is restored, and thus spin degeneracy of the bands at each valley takes place. Here spin and valley are not coupled, which means that under incidence of polarized light there would be generation of spin population at **K** and **K′**, giving a net spin polarization, but no valley polarization.

Table II shows a comparison of some of the highest reported percentage values of $|\mathcal{D}^z|$ for surface and bulk systems. We can see that one-monolayer MoS₂ structure as well as the bulk CdSe and the Si(111)-As 1 × 1 surface reach 100% of spin polarization at the visible-range photon energies of 2.01, 1.8, and 2.2 eV, respectively. It is worth mentioning that both centrosymmetric bulk MoS₂ and Si media present a net spin polarization. Their corresponding maximum is within the visible and within the ultraviolet photon frequency range, correspondingly.

It is possible to obtain the degree of spin polarization near the band edge through the use of a two-band model [6], or just at the band edge through an analysis of the energy level diagram [10]. Indeed, those models will be suitable to capture the spin polarization result of the monolayer MoS₂ structure at the band edge, but they will have the limitation of obtaining the spin polarization far from it or decomposing the spectrum into contributions from different transitions. In contrast, the full-band structure calculation that we have performed allows us to obtain the spin polarization within a wide range of frequencies well above the band gap and to separate different transition contributions to the total spectrum. In order to appreciate the numerical contribution of the top valence and bottom conduction bands to the spin polarization near the band edge, in the spectrum for $\zeta^{abc}(\omega)$ [Eq. (3)], we have just considered those spin injection contributions that
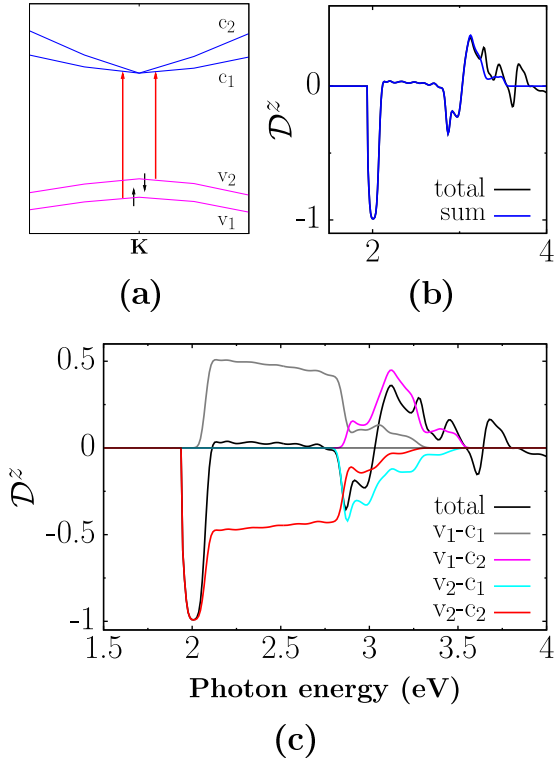
(a)

(b)

(c)

FIG. 6. (a) Scheme showing the two higher valence and two lowest conduction bands of the monolayer MoS_2 structure. (b) Total degree of spin polarization spectra of the monolayer MoS_2 structure and the respective "sum" spectrum that is the sum of those spectra shown in (c), which come from the four different possible transitions between any of the two higher valence bands with any of the two lowest conduction bands.

come from the two top valence and two bottom conduction bands [see Fig. 6(a)]. The corresponding $\mathcal{D}^z$ spectrum labeled "sum" in Fig. 6(b) will comprise the four contributions shown in Fig. 6(c) that come from transitions that take place between any of the two higher valence and any of the two lowest conduction bands. In Figs. 6(b) and 6(c), we also show the total $\mathcal{D}^z$ spectrum for comparison. We can see that it is just enough to consider the contributions of the two top valence and two bottom bands to obtain the respective spectrum for $\mathcal{D}^z$ of the monolayer MoS_2 structure up to the photon energy at around 3.2 eV. Furthermore, the rise of the feature of $\mathcal{D}^z$ at around 2.01 comes mainly from transitions between the highest valence and the second lower conduction band. Here, under optical excitation, the optical field is injecting spin down electrons from v_2 to c_2 bands [see Fig. 6(a)]. On the other hand, the decrease of this feature as the energy increases comes along with an increase of the respective spectrum contribution coming from transitions taking place from v_1 to c_1 bands. Hence it is sufficient to consider contributions from the two top valence and two top conduction bands to capture the result for $\mathcal{D}^z$ at around the **K** point. Within the energy range from 2.2 to 2.7 eV, the contributions coming from spin injection rates of spin-down and spin-up electrons are almost equal but opposite in sign, resulting in an almost zero value for the $\mathcal{D}^z$ spectrum.

In order to have an account of the contribution of each local site to the the $\mathcal{D}^z$ spectrum for the centrosymmetric
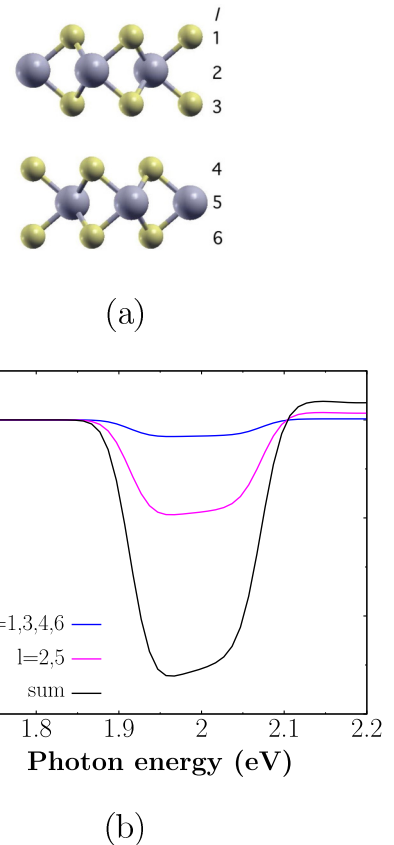

(a)

(b)

FIG. 7. (a) Side view of the two-monolayer MoS_2 structure. (b) Spectra of the spin generation rate tensor component ζ^{zxy} as a function of the atomic layer for the two-monolayer MoS_2 structure, under incidence of circularly polarized light. The curve labeled "sum" is the respective total spectrum corresponding to the sum of the six atomic-layer contributions.

two-monolayer MoS_2 structure, we have followed the formalism of Ref. [14] and calculated spectra of the spin generation rate tensor component ζ^{zxy} as a function of the atomic layer. We show the respective spectra in Fig. 7, wherein we have just plotted the structure of the spectra that comes from transitions at around around 2 eV. We observe that all six layers have nonzero contributions to the spin generation rate tensor component. The contributions to the ζ^{zxy} spectrum corresponding to S atomic layers 1, 3, 4, and 6 are equal, as well as the respective contributions of the Mo layers 2 and 5. All layers contribute almost in the whole frequency range with the same sign to the spin generation rate spectrum. There the sum of the respective six atomic-layer contributions to the ζ^{zxy} spectrum is also shown. Furthermore, we can see that the main contributions to the feature found at around 2.0 eV of the spin generation rate total spectrum are those coming from Mo layers. Although there is a larger feature at around 2.7 eV for the spin generation rate, once it is divided by the carrier injection rate, $|\mathcal{D}^z|$ gives the value of 0.39 as it is shown in Fig. 5(a).

C. Current injection

We have also calculated spectra for the injection current response of the studied MoS_2 structures. The
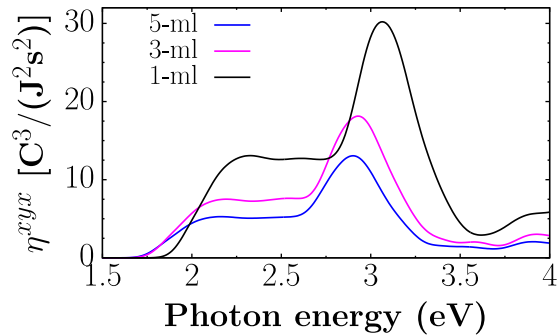
FIG. 8. Spectra of the injection current tensor component, η^{xyx}, for monolayer systems of MoS$_2$ comprising one, three, and five monolayers, respectively.

noncentrosymmetric monolayer MoS$_2$ structures have the nonzero components η^{xxz}, η^{yyz}, and η^{xyx}. The first two are practically zero, and we show in Fig. 8 spectra for the latter injection current tensor component, η^{xyx}, for each of the studied MoS$_2$ structures. We can observe that, under incidence of circularly polarized light, there would be an optical injection current along the x direction for noncentrosymmetric monolayer MoS$_2$ structures, that is, for structures with an odd number of layers. Meanwhile, there is no injection current generation in both the monolayer MoS$_2$ structures with an even number of layers and the centrosymmetric bulk structure. The maximum of the spectrum for the one-monolayer structure is at around 3.1 eV, and it redshifts as the number of layers increases. In general, the magnitude of the spectrum in the whole frequency range decreases as the number of layers increases in the MoS$_2$ structure, approaching the bulk zero value. In order to obtain an estimation of the current density that can be generated, we consider the relation $J_{inj} \propto 4\tau\eta|E_0|$, where τ is the carrier relaxation time. Considering an incident field with intensity of 100 mW/cm^2, the intraband carrier relaxation time of 500 fs

[55], and the calculated magnitude of 10 C^3/(J^{2}s^2) for η, we obtain an estimation for the current density of 0.4 nA/cm^2. This amount of current density is of the order of those of dark currents generated in some photodiodes [56,57]. Since the current signal scales linearly with the field intensity, it might be expected that, for higher intensities, the generation of measurable current densities would be possible.

VI. CONCLUSIONS

We have performed *ab initio* calculations for the optical injection of current and spin on bulk and n-monolayer MoS$_2$ systems. On the one hand, our calculations for the injection current in few monolayer MoS$_2$ structures show that, with incident light circularly polarized on the plane of the monolayer, measurable current densities can be optically generated. On the other hand, we have also found that, under incidence of circularly polarized light, it is possible to inject spin-polarized electrons to the conduction bands along the direction that is perpendicular to the plane of the monolayers of MoS$_2$. The maximum degree of spin polarization of the injected electrons in a monolayer MoS$_2$ structure is 100% at the **K** valley. The addition of the valley degree of freedom allows having control of the spin polarized carrier in a specific region of the BZ. The maximum degree of spin polarization for each of the n-monolayer MoS$_2$ structures decreases as the number of monolayers increases, reaching a percentage value of 70%. Hence it is possible to coherently control and generate spin polarized electrons in both bulk and monolayer MoS$_2$ structures. Thus we conclude that, according to our results, monolayer MoS$_2$ structures are optimal for spintronics applications.

[1] Z. M. Wang, MoS$_2$, *Material Physics, and Devices* (Springer, New York, 2014).

[2] C. Lee, H. Yan, L. E. Brus, T. F. Heinz, J. Hone, and S. Ryu, ACS Nano **4**, 2695 (2010).

[3] K. F. Mak, C. Lee, J. Hone, J. Shan, and T. F. Heinz, Phys. Rev. Lett. **105**, 136805 (2010).

[4] O. Gunawan, Y. P. Shkolnikov, K. Vakili, T. Gokmen, E. P. De Poortere, and M. Shayegan, Phys. Rev. Lett. **97**, 186404 (2006).

[5] W. Yao, D. Xiao, and Q. Niu, Phys. Rev. B **77**, 235406 (2008).

[6] D. Xiao, G.-B. Liu, W. Feng, X. Xu, and W. Yao, Phys. Rev. Lett. **108**, 196802 (2012).

[7] T. Cao, G. Wang, W. Han, H. Ye, C. Zhu, J. Shi, Q. Niu, P. Tan, E. Wang, B. Liu, and J. Feng, Nat. Commun. **3**, 887 (2012).

[8] R. A. Muniz and J. E. Sipe, Phys. Rev. B **91**, 085404 (2015).

[9] M. I. Dyakonov and V. I. Perel, in *Optical Orientation*, edited by F. Meier and B. P. Zakharchenya (Elsevier, New York, 1984), Chap. 2.

[10] F. Nastos, J. Rioux, M. Strimas-Mackey, B. S. Mendoza, and J. E. Sipe, Phys. Rev. B **76**, 205113 (2007).

[11] J. L. Cabellos, C. Salazar, and B. S. Mendoza, Phys. Rev. B **80**, 245204 (2009).

[12] J. Rioux and J. E. Sipe, Phys. Rev. B **81**, 155215 (2010).

[13] N. Arzate, R. A. Vázquez-Nava, and B. S. Mendoza, Phys. Rev. B **90**, 205310 (2014).

[14] B. S. Mendoza and J. L. Cabellos, Phys. Rev. B **85**, 165324 (2012).

[15] F. Nastos and J. E. Sipe, Phys. Rev. B **74**, 035201 (2006).

[16] R. D. R. Bhat and J. E. Sipe, Phys. Rev. B **72**, 075205 (2005).

[17] D. Côte, N. Laman, and H. M. van Driel, Appl. Phys. Lett. **80**, 905 (2002).

[18] J. E. Sipe and A. I. Shkrebtii, Phys. Rev. B **61**, 5337 (2000).

[19] J. M. Fraser, A. I. Shkrebtii, J. E. Sipe, and H. M. van Driel, Phys. Rev. Lett. **83**, 4192 (1999).

[20] A. Haché, Y. Kostoulas, R. Atanasov, J. L. P. Hughes, J. E. Sipe, and H. M. van Driel, Phys. Rev. Lett. **78**, 306 (1997).

[21] R. Atanasov, A. Haché, J. L. P. Hughes, H. M. van Driel, and J. E. Sipe, Phys. Rev. Lett. **76**, 1703 (1996).

[22] N. Laman, A. I. Shkrebtii, J. E. Sipe, and H. M. van Driel, Appl. Phys. Lett. **75**, 2581 (1999).

[23] T.-R. Chang, H. Lin, H.-T. Jeng, and A. Bansil, Sci. Rep. **4**, 6270 (2014).

[24] H. Zeng, J. Dai, W. Yao, D. Xiao, and X. Cui, Nat. Nanotechnol. **7**, 490 (2012).

[25] K. F. Mak, K. He, J. Shan, and T. F. Heinz, Nat. Nanotechnol. **7**, 494 (2012).

[26] W. S. Yun, S. W. Han, S. C. Hong, I. G. Kim, and J. D. Lee, Phys. Rev. B **85**, 033305 (2012).

[27] L. Liu, S. B. Kumar, Y. Ouyang, and J. Guo, IEEE Trans. Electron Devices **58**, 3042 (2011).

[28] L. Debbichi, O. Eriksson, and S. Lebègue, Phys. Rev. B **89**, 205311 (2014).

[29] X. Gonze *et al.*, Comput. Mater. Sci. **25**, 478 (2002); X. Gonze, Zeitschrift für Kristallographie - Crystalline Materials **220**, 558 (2005).

[30] C. Hartwigsen, S. Goedecker, and J. Hutter, Phys. Rev. B **58**, 3641 (1998).

[31] R. Sakuma, C. Friedrich, T. Miyake, S. Blügel, and F. Aryasetiawan, Phys. Rev. B **84**, 085144 (2011).

[32] I. Aguilera, C. Friedrich, and S. Blügel, Phys. Rev. B **88**, 165136 (2013).

[33] I. Aguilera, C. Friedrich, G. Bihlmayer, and S. Blügel, Phys. Rev. B **88**, 045206 (2013).

[34] I. Aguilera, C. Friedrich, and S. Blügel, Phys. Rev. B **91**, 125129 (2015).

[35] C. Li, A. J. Freeman, H. J. F Jansen, and C. L. Fu, Phys. Rev. B **42**, 5433 (1990).

[36] R. Del Sole and R. Girlanda, Phys. Rev. B **48**, 11789 (1993).

[37] H. Hübener, E. Luppi, and V. Véniard, Phys. Rev. B **83**, 115205 (2011).

[38] H. Peelaers, B. Partoens, M. Giantomassi, T. Rangel, E. Goossens, G.-M. Rignanese, X. Gonze, and F. M. Peeters, Phys. Rev. B **83**, 045306 (2011).

[39] H.-P. Komsa and A. V. Krasheninnikov, Phys. Rev. B **86**, 241201 (2012).

[40] T. Cheiwchanchamnangij and W. R. L. Lambrecht, Phys. Rev. B **85**, 205302 (2012).

[41] A. Ramasubramaniam, Phys. Rev. B **86**, 115409 (2012).

[42] F. Hüser, T. Olsen, and K. S. Thygesen, Phys. Rev. B **88**, 245309 (2013).

[43] H. Shi, H. Pan, Y.-W. Zhang, and B. I. Yakobson, Phys. Rev. B **87**, 155304 (2013).

[44] D. Y. Qiu, F. H. da Jornada, and S. G. Louie, Phys. Rev. Lett. **111**, 216805 (2013).

[45] S. W. Han, H. Kwon, S. K. Kim, S. Ryu, W. S. Yun, D. H. Kim, J. H. Hwang, J.-S. Kang, J. Baik, H. J. Shin, and S. C. Hong, Phys. Rev. B **84**, 045409 (2011).

[46] A. Splendiani, L. Sun, Y. Zhang, T. Li, J. Kim, C.-Y. Chim, G. Galli, and F. Wang, Nano Lett. **10**, 1271 (2010).

[47] A. R. Beal and H. P. Hughes, J. Phys. C **12**, 881 (1979).

[48] C. Delerue, G. Allan, and M. Lannoo, Phys. Rev. Lett. **90**, 076803 (2003).

[49] R. Coehoorn, C. Haas, and R. A. de Groot, Phys. Rev. B **35**, 6203 (1987).

[50] Y. Zhang, H. Li, H. Wang, R. Liu, S.-L. Zhang, and Z.-J. Qiu, ACS Nano **9**, 8514 (2015).

[51] X. Zhang, Q. Liu, J.-W Luo, A. J. Freeman, and A. Zunger, Nat. Phys. **10**, 387 (2014).

[52] B. Partoens, Nat. Phys. **10**, 333 (2014).

[53] E. I. Rashba, Sov. Phys.-Solid State **2**, 1109 (1960).

[54] G. Dresselhaus, Phys. Rev. **100**, 580 (1955).

[55] D. Kozawa, R. Kumar, A. Carvalho, K. K. Amara, W. Zhao, S. Wang, M. Toh, R. M. Ribeiro, A. H. Castro Neto, K. Matsuda, and G. Eda, Nat. Commun. **5**, 4543 (2014).

[56] N. Biyikli, O. Aytur, I. Kimukin, T. Tut, and E. Ozbay, Appl. Phys. Lett. **81**, 3272 (2002).

[57] M. Binda, A. Iacchetti, D. N. L. Beverina, M. Sassi, and M. Sampietro, Appl. Phys. Lett. **98**, 073303 (2011).